Color line search for illuminant estimation in real-world scenes

Thomas M. Lehmann and Christoph Palm

Institute of Medical Informatics, Aachen University of Technology, 52057 Aachen, Germany

Received January 2, 2001; revised manuscript received April 23, 2001; accepted April 24, 2001

The estimation of illuminant color is mandatory for many applications in the field of color image quantification. However, it is an unresolved problem if no additional heuristics or restrictive assumptions apply. Assuming uniformly colored and roundly shaped objects, Lee has presented a theory and a method for computing the scene-illuminant chromaticity from specular highlights [H. C. Lee, J. Opt. Soc. Am. A **3**, 1694 (1986)]. However, Lee's method, called image path search, is less robust to noise and is limited in the handling of microtextured surfaces. We introduce a novel approach to estimate the color of a single illuminant for noisy and microtextured images, which frequently occur in real-world scenes. Using dichromatic regions of different colored surfaces, our approach, named color line search, reverses Lee's strategy of image path search. Reliable color lines are determined directly in the domain of the color diagrams by three steps. First, regions of interest are automatically detected around specular highlights, and local color diagrams are computed. Second, color lines are determined according to the dichromatic reflection model by Hough transform of the color diagrams. Third, a consistency check is applied by a corresponding path search in the image domain. Our method is evaluated on 40 natural images of fruit and vegetables. In comparison with those of Lee's method, accuracy and stability are substantially improved. In addition, the color line search approach can easily be extended to scenes of objects with macrotextured surfaces.

OCIS codes: 330.1690, 150.2950, 100.2000.

1. INTRODUCTION

The understanding of color constancy is important in psychology as well as digital image processing. Color constancy is the attempt to derive intrinsic reflectance properties of objects, which are independent of extrinsic parameters such as illumination, viewing direction, surface orientation, and surrounding colors. Although not perfect, human perception allows illumination-independent color description. Numerous experimental studies have been performed to obtain insights into this phenomenon and to develop models that explain the mechanisms of human illuminant adjustment.[1–6] In this context, the roles of scene background,[1,2] other image surfaces,[3] and human color memory[4] have been studied.

A common approach to color constancy is the estimation of physical parameters from the output of photoreceptors, e.g., illuminant spectrum and surface reflectance spectrum.[6–12] Obviously, the correct estimation of spectra is sufficient but not necessary to solve the color constancy problem.[7] The measurement of color spectra with few sensors is similar both for the human visual system and for technical color imaging. Nevertheless, color constancy in human vision requires an understanding of human perception, while color constancy in image processing is tantamount to reliable estimation of reflectance properties[8,9] or scene parameters,[13,14] which are independent of the scene's illumination. In this paper, we focus on the technical point of view.

Most frequently, simple imaging geometries with uniform diffuse and spatial illumination as well as flat surfaces without luster have been assumed.[6,7] Alternatively, low-dimensional linear models with fixed basis functions are used to describe the surface and illuminant spectra of real-world scenes.[15] For such models, Maloney and Wandell[15] have proven that only $N - 1$ descriptors of surface reflectance can be uniquely recovered from a scene that is illuminated by a single illuminant using a single-view visual system with N sensors. In other words, the trichromatic human visual system and any three-chip CCD camera are able to recover only two surface descriptors. This is insufficient for an appropriate representation of natural surfaces. Increasing the number of descriptors requires the inversion of an underconstrained nonlinear system of equations. Reliable estimations have been achieved by Brainard and Freeman[7] using a Bayesian framework with a special loss function.

The use of additional information provides further descriptors for each surface. In simple approaches, color charts[16] or patches with neutral spectral reflection are added to the scene. Ho *et al.*[9] have applied the theory of chromatic aberration to determine the illuminant. D'Zmura and Iverson[6] inspected several views of the surface under different illumination conditions in order to estimate surface and illuminant parameters. However, additional information is obtainable in only a limited number of applications. For example, in medical diagnostics, charts and patches are inapplicable to the patient, and additional examinations will increase inconvenience or pain.[17,18]

Other approaches are based on restrictive suppositions. For instance, Buchsbaum[19] and Land[20] have applied the gray-world assumption. D'Zmura and Lennie[5] and Lee[21] have evaluated color changes on highlights. Introducing the quarter-circle analysis, Tominaga and Wandell[10,11] focused on three-dimensional objects, where the reflectance was described by the dichromatic reflection model.[12,22]

0740-3232/2001/112679-13$15.00

For these surfaces, Brill[23] has introduced the concept of rank-2 fields. This approach requires a precise segmentation of the image. In real-world scenes, disturbing effects have to be considered. Usually, the illumination cannot be controlled. Furthermore, microtextured surfaces and noisy pixels violate the basic assumption of homogeneous objects, which complicates rank-2 segmentation. Therefore methods are required to determine the illuminant color without segmentation.

Working from the dichromatic reflection model, Lee[21] has introduced a method for computing the scene-illuminant chromaticity from specular highlights of colored objects. All colors are normalized on the values of the red channel. In those red diagrams, the dichromatic lines of colored objects intersect at one point, determining the illumination color. This approach was generalized later for the three-dimensional color histogram, where different color planes intersect in a certain line.[10] Although Lee's method performs sufficiently well on synthetic images of spheres, its application to real-world scenes is sensitive to noise or inhomogeneities such as textured surfaces.

In this paper, we extend Lee's basic idea to determine the intersection of color lines from the red diagram to the *rg* diagram, and, more essentially, we propose a novel method to locate appropriate color lines directly in the domain of the color diagram. Lee's method of image path search (IPS) (see Subsection 2.B) is performed in the image domain. Color values are collected along a certain direction in the image, starting at a specular highlight. Paths resulting from different objects are transformed in the color diagram to determine their intersection. In contrast, our novel approach of color line search (CLS) (see Subsection 2.C) directly searches for straight lines in color diagrams. The diagrams are obtained from image regions located around specular highlights on different objects. All hypotheses are retransformed into the image domain to test their validity. The intersection of valid color lines is then computed once more in the color diagram.

2. ILLUMINANT COLOR ESTIMATION

A. Dichromatic Reflection Model

According to the dichromatic reflection model,[22] each color vector $(R,G,B)^{\mathrm{T}}$ is determined by a linear combination of surface reflection $(R_s,G_s,B_s)^{\mathrm{T}}$ and body reflection $(R_b,G_b,B_b)^{\mathrm{T}}$:

$$\begin{pmatrix} R \\ G \\ B \end{pmatrix} = w_s \begin{pmatrix} R_s \\ G_s \\ B_s \end{pmatrix} + w_b \begin{pmatrix} R_b \\ G_b \\ B_b \end{pmatrix}. \tag{1}$$

The weights w depend only on the geometry of the imaging system, whereas the color vectors result from the multiplication of the distribution of the irradiance spectrum and the reflectances of surface and body before tristimulus integration, $s(\lambda)$, $\beta_s(\lambda)$, and $\beta_b(\lambda)$, respectively. A neutral surface equally reflects all wavelengths λ. This yields $\beta_s(\lambda) = \beta_s$ and allows us to rewrite Eq. (1) for dichromatic reflection:

$$\begin{pmatrix} R \\ G \\ B \end{pmatrix} = w_s \beta_s \begin{pmatrix} \int_\lambda s(\lambda)\bar{r}(\lambda)\mathrm{d}\lambda \\ \int_\lambda s(\lambda)\bar{g}(\lambda)\mathrm{d}\lambda \\ \int_\lambda s(\lambda)\bar{b}(\lambda)\mathrm{d}\lambda \end{pmatrix} + w_b \begin{pmatrix} \int_\lambda \beta_b(\lambda)s(\lambda)\bar{r}(\lambda)\mathrm{d}\lambda \\ \int_\lambda \beta_b(\lambda)s(\lambda)\bar{g}(\lambda)\mathrm{d}\lambda \\ \int_\lambda \beta_b(\lambda)s(\lambda)\bar{b}(\lambda)\mathrm{d}\lambda \end{pmatrix}, \tag{2}$$

where $\bar{r}(\lambda)$, $\bar{g}(\lambda)$, and $\bar{b}(\lambda)$ determine the responsiveness of the red, green, and blue color sensors, respectively. Since the responsiveness of each sensor is strictly positive in a finite interval, the integration in Eq. (2) becomes definite. Applying the first generalized mean-value theorem of the integral calculus, $\int_a^b k(x)l(x)\mathrm{d}x = \kappa\int_a^b l(x)\mathrm{d}x$, and replacing the tristimulus integration of $s(\lambda)$ by $(s^R,s^G,s^B)^T$ yield

$$\begin{pmatrix} R \\ G \\ B \end{pmatrix} = w_s\beta_s \begin{pmatrix} s^R \\ s^G \\ s^B \end{pmatrix} + w_b \begin{pmatrix} \beta_b^R s^R \\ \beta_b^G s^G \\ \beta_b^B s^B \end{pmatrix}. \tag{3}$$

1. Red Diagram

According to Lee,[21] the varying weights of body and surface reflection form a straight color line in the red-normalized diagram. If $R \neq 0$, G, and B are all different, we obtain

$$\frac{B}{R} = a\frac{G}{R} + b, \tag{4}$$

where slope a and ordinary intercept b are given from Eq. (3) by

$$a = \frac{s^B}{s^G}\frac{\beta_b^B - \beta_b^R}{\beta_b^G - \beta_b^R}, \qquad b = \frac{s^B}{s^R}\frac{\beta_b^G - \beta_b^B}{\beta_b^G - \beta_b^R} \tag{5}$$

(see Appendix A). Note that the parameters a and b depend only on the irradiance spectrum $s(\lambda)$ and the color of body reflection $\beta_b(\lambda)$.

2. rg Diagram

The normalization of colors to the red channel only, as proposed with Eq. (4) by Lee, is asymmetric and particularly susceptible to noise in the red channel. According to the CIE *XYZ* system, the chromaticity *xy* diagram is defined by normalization on the sum of X, Y, and Z. Such normalization is similarly used for the camera-specific RGB color space. Let us define the parameters

$$r = \frac{R}{R+G+B}, \qquad g = \frac{G}{R+G+B}. \tag{6}$$

Hence Eq. (3) results in

$$g = a'r + b', \tag{7}$$

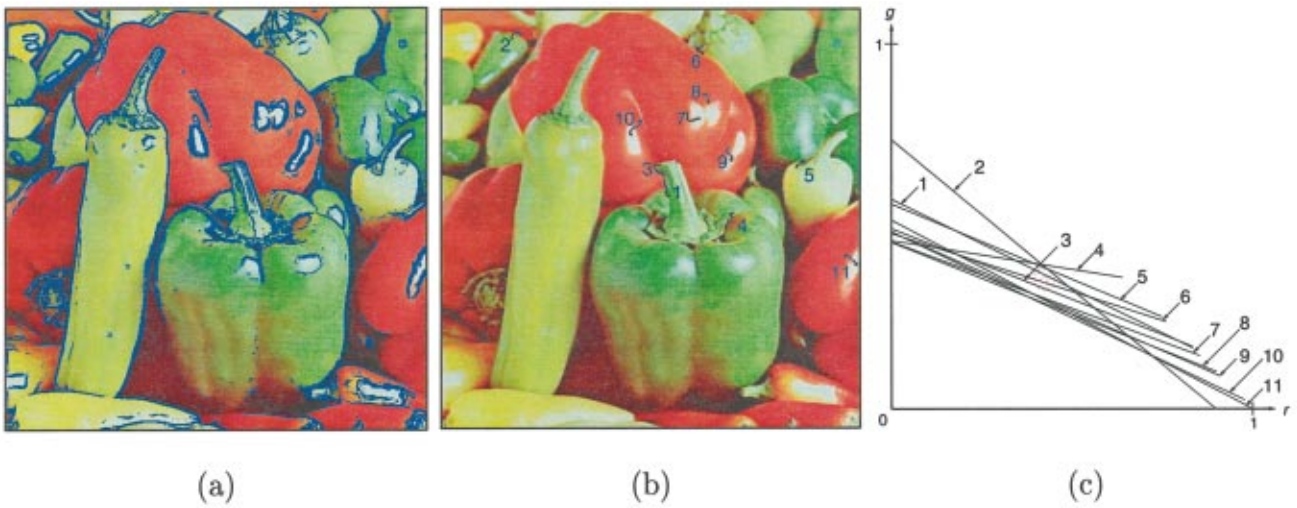

Fig. 1. (a) The color edges obtained by the Laplacian-of-Gaussian within each band (512 × 512 pixels) of the standard image "peppers" are marked in blue. They are used as starting points for the IPS algorithm. (b) Only 11 paths remain for minimal lengths of 7 and 10 pixels at the ascending and descending parts of each path, respectively. (c) The intersection of corresponding color lines within the *rg* diagram determines the scene-illuminant chromaticity.

$$a' = -\frac{1 - \dfrac{s^B(\beta_b^B - \beta_b^G)}{s^R(\beta_b^G - \beta_b^R)}}{1 + \dfrac{s^B(\beta_b^B - \beta_b^R)}{s^G(\beta_b^G - \beta_b^R)}}, \qquad b' = \frac{1}{1 + \dfrac{s^B(\beta_b^B - \beta_b^R)}{s^G(\beta_b^G - \beta_b^R)}}$$

(see Appendix B). Again, slope a' and intercept b' depend only on reflectance properties and not on the parameter w. Supposing dissimilar object and illuminant colors, two objects that differ in spectral emission yield color lines that intersect in the *rg* diagram at $(r, g) = (p_r, p_g)$, with

$$p_r = \frac{s^R}{s^R + s^G + s^B}, \qquad p_g = \frac{s^G}{s^R + s^G + s^B} \tag{8}$$

(see Appendix C).

B. Lee's Method of Image Path Search

1. Principle

The basic idea of Lee's image path search (IPS) algorithm is to collect normalized colors along a path in the image domain from the body to the surface reflection color. According to the dichromatic reflection model, a straight line is formed in both the red diagram and the *rg* diagram. The starting point of the path is supposed to be located at changes of color. These color edges are determined by the zero crossings of the Laplacian-of-Gaussian filtered color bands [Fig. 1(a)]. Since suitable paths must cross a color edge, they are split into an ascending and a descending part, each of which starts at the color edge point [Fig. 1(b)]. The color changes correlate with changes in brightness, which is high with respect to the surface reflection but rather low concerning body reflection. Therefore the path route of the IPS is controlled by the object's brightness instead of its chromaticity (which is still unknown at this moment). Along the ascending and descending parts, the normalized colors of the image are collected. Since smooth and monochrome objects are assumed, each set forms a straight line in the *rg* diagram [Fig. 1(c)]. If both parts significantly differ in slope, e.g., at the border between different objects, they are disregarded. Each color edge pixel within the image is considered a starting point for the IPS algorithm. If two color lines obtained are similar, e.g., at a change of surface and body reflection, they are merged. In addition, short paths are suppressed. If two or more different paths are determined, the illuminant color is fixed at the point of intersection.

2. Remarks

In the original paper,[21] Lee successfully tested the method of IPS on a synthetic image of two spheres with ideal reflection properties. However, this proves the usefulness of the idea rather than its applicability to real-world scenes, such as the public-domain image "peppers" (Figs. 1–3). Although its calibration is undefined and one might suspect that the image metric is not in linear exposure space, the peppers image has been used as a standard in many research establishments.

In general, real-world images show noisy or (slightly) inhomogeneous objects, resulting in variations of brightness and color that may restrict or even violate the dichromatic reflection model. Furthermore, the highlights are often very small, and therefore the ascending part of the path is too short for a robust IPS. Another problem arises from mutual illumination at object borders. One object illuminates the other, and vice versa. Funt and Drew[24] have shown this interreflection to agree with the dichromatic reflection model, and, consequently, paths at interreflection borders are accepted by Lee's algorithm [e.g., see paths 1–6 in Fig. 1(b)]. The corresponding color lines do not belong to the scene-illuminant chromaticity and cause major detection errors; e.g., the point of intersection is mislocated in Fig. 1(c).

C. Our Approach of Color Line Search

The problems indicated above are mostly related to local data irregularities in the image domain, where the detec-

tion of color lines by Lee's IPS method takes place. To overcome this drawback, we apply a reversing strategy. With the use of our color line search (CLS) approach, straight lines are detected directly in the *rg* diagram before they are retransformed and verified in the image domain by an IPS-related algorithm. This essentially improves the entire algorithm. The CLS method is independent of starting points, which formerly have had to be selected in a noisy image. Furthermore, the CLS method avoids all problems related to interreflection borders. It is reliable and capable of processing partly interrupted paths in the image domain, which often result from microtextured objects in real-world scenes.

1. Determination of Regions of Interest

The detection of straight color lines referring to the *rg* diagram of a multicolored image [Fig. 2(a)] is not applicable because of the high densities in its color histogram [Fig. 2(b)]. Therefore *rg* diagrams are computed for small regions of interest (ROIs), where color changes from body to surface reflection are expected. These color changes mostly occur in the surrounding of specular highlights [Fig. 2(c)]. Specular highlights are coarsely characterized by local coincidence of intense brightness and unsaturated color:

$$I = \frac{R + G + B}{3} > \frac{1}{2} I_{\max},$$

$$S = 1 - \frac{\min(R, G, B)}{I} < \frac{1}{2} S_{\max}, \tag{9}$$

where $I_{\max}$ and $S_{\max}$ denote the highest intensity I and the highest saturation S in the image, respectively. Note that the number as well as the centers of gravity of the detected highlights remains unchanged for a wide range

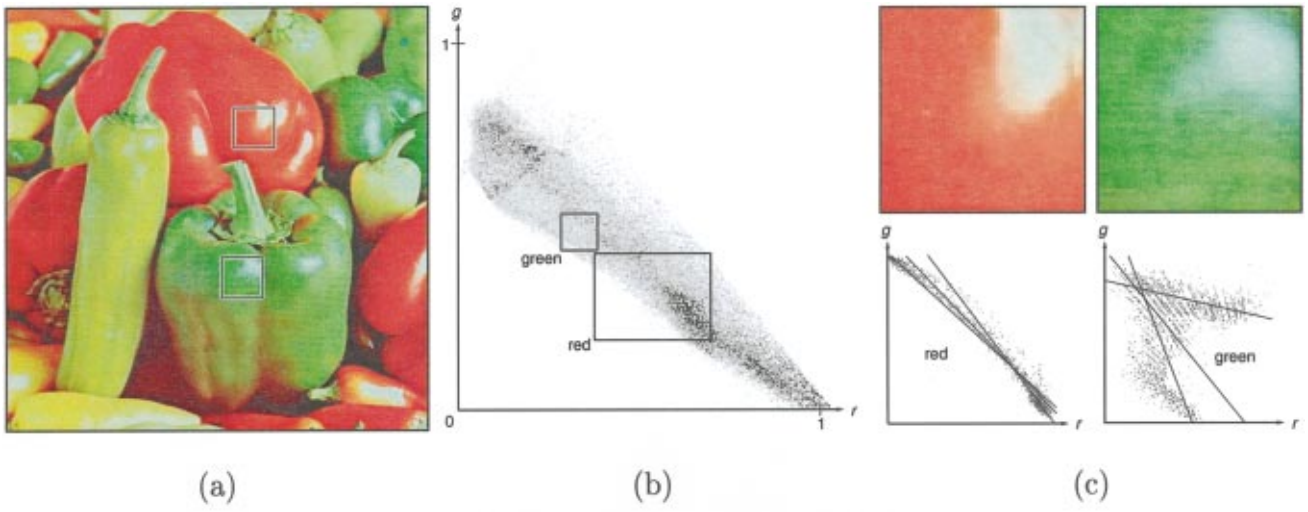

Fig. 2. (a) Two regions of interest (ROIs) are emphasized in the peppers standard image. The green pepper shows a microtextured surface, whereas the red one's is rather homogeneous. (b) The high densities of the *rg* diagram obtained from the entire image do not allow the identification of individual straight lines. (c) In contrast, such lines can be seen in the zoomed *rg* diagrams obtained only from the ROIs. The three best lines have been determined by a Hough transform.

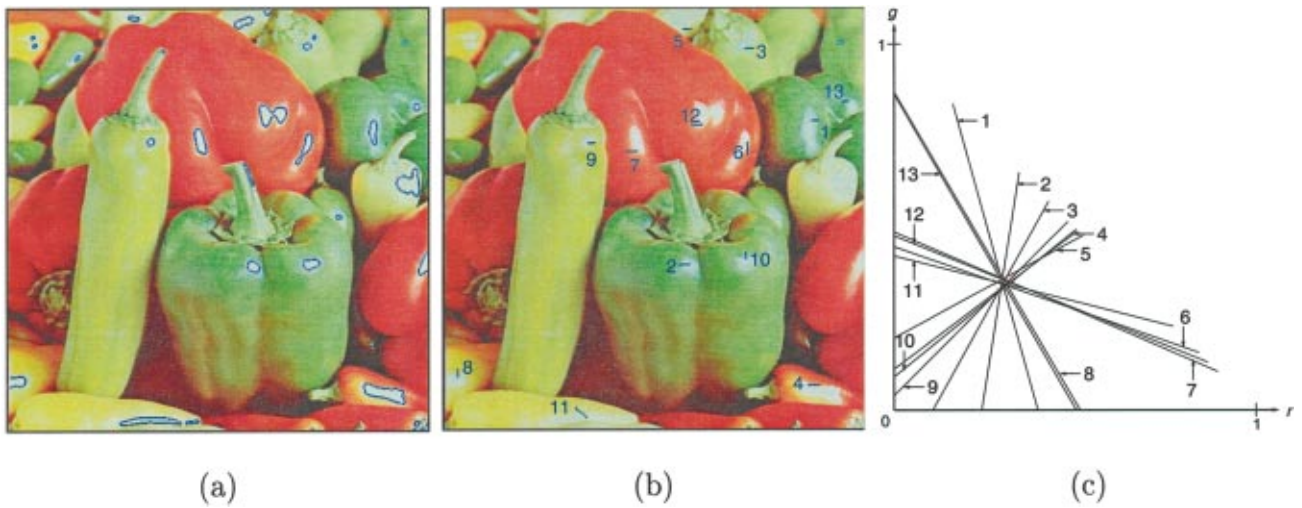

Fig. 3. (a) Regions of specular highlights that have been determined by thresholding saturation and brightness are marked in the peppers standard image. (c) With a CLS applied, 13 valid color lines have been detected. Note that all lines meet in a sharply focused point of intersection. The corresponding image paths that are built to check the consistency are displayed in (b).

of thresholds. In addition, errors of this simple method are recognized and subsequently rejected by applying a consistency check (see Subsection 2.C.3). For each detected highlight, four ROIs are placed such that their corners meet in the center of the highlight.

2. Detection of Color Line Proposals

Color line proposals are determined within the *rg* diagram of each ROI by applying the Hough transform.[25] The Hough transform considers all lines passing through the current pixel of a binary image. Lines are characterized by their slope and intersection. These parameters are spanning the Hough domain, which is also referred to as the accumulator array. During the transform, each positive pixel in the binary image causes the increase of all slope–intercept cells in the accumulator array, which are related to possible lines. A final maximum detection in the Hough domain directly locates the straight line in the binary image that comes with the largest number of contributing pixels. The major advantage of the Hough transform is its independence of local disturbances of lines. Only the total number of pixels contributing to a line is important, not their relative positions.

Since the values of slope become infinite when color lines are parallel to the vertical axis, they cannot be parameterized if the Hough domain is defined by slope and intercept. In our implementation, the Hessian standard form is applied to parameterize straight lines by their distance to the origin and the angle of the distance vector. This results in sinusoidal curves in the Hough domain.[25] After all pixels are transformed from the *rg* diagram of any ROI, local maxima are determined. With the use of Eq. (7), the coordinates of the maxima determine a' and b' of straight lines in the *rg* diagram. Note that the height of a maximum is directly related to the number of points forming the straight line in the *rg* diagram. Hence a few lines with the most points serve as color line proposals of each ROI to indicate the illuminant color at the image object. Figure 2(c) shows three hypotheses in each of the *rg* diagrams of the two ROIs from Fig. 2(a).

3. Consistency Check

It is obvious that the number of points cannot be the unique criterion to select reliable dichromatic color lines. Therefore each line proposal is checked within the corresponding ROI according to its consistency with the dichromatic reflection model. For each color line proposal, an image path inside the ROI is searched for, such that the normalized colors lie on the current color line. The order of colors along the path is important. We assume smooth surfaces without abrupt changes of the surface's normal direction. Processing the colors on the line in ascending order, a reliable path must be rectilinear without sharp edges or U turns. However, not all colors of the color line have to occur on the image path. The fact that we search for a specific color in a specific direction enables us to relax Lee's condition of direct neighborhood for image path elements. Consequently, we accept gaps of 2 or less pixels to jump over noise or to connect patches of microtextured surfaces. Since each path must remain on the same surface, larger gaps demand more sophisticated consistency rules, which are not implemented yet.

If the length of the resulting path exceeds a threshold, the dichromatic reflection model is satisfied and the corresponding straight line is selected as a valid color line describing the current highlight. In other words, the length of the corresponding image path is used as a criterion for the validity of the reflection model for the current color line. Figure 3(a) shows the highlights within the peppers image that is used for our CLS algorithm. Valid image paths with an approved CLS hypothesis are marked in Fig. 3(b). For the CLS approach, color lines obviously intersect at a distinctly focused point [Fig. 3(c)].

D. Estimation of the Intersection Point

The color lines of different objects with slope a' and intercept b' have now been determined by applying either the IPS or the CLS method [Fig. 1(c) or 3(c), respectively]. However, the intersection of valid color lines from real-world scenes cannot be located exactly. The Hough transform is used again to estimate the point of intersection. For all color lines, the parameters (a', b') are transformed into the Hough domain. If all color lines perfectly meet within a distinct point of intersection, the Hough-transformed parameters form a unique straight line. For real-world scenes, the straight line that fits best all data points in the Hough space is computed by the Karhunen–Loève transform. Note that this equals the least-squares regression of the distances between all points and the line. From Eqs. (7) and (8), we obtain slope $-p_r$ and ordinate intercept p_g of this line in the Hough domain:

$$b' = -p_r a' + p_g . \tag{10}$$

E. Summary of the Algorithm

Assuming the dichromatic color model, the problem of illuminant estimation in real-world scenes is reduced to finding the intersection point of valid color lines in the *rg* diagram. Applying the CLS method, we determine color line proposals by Hough transform of *rg* diagrams representing ROIs at specular highlights [Fig. 3(a)]. They are evaluated by path-searching the image domain [Fig. 3(b)]. Valid color lines are represented by their slope and intercept in the Hough domain. The Karhunen–Loève transform is applied to estimate the best-fitting straight line in the Hough domain, which equals the regression of the point of intersection in the *rg* diagram [Fig. 3(c)]. A pseudocode of the CLS algorithm is provided in Fig. 4.

3. VALIDATION OF THE COLOR LINE SEARCH METHOD

Lee's rather general evaluation was based on an artificial image of spheres that was computer generated according to the dichromatic reflectance model.[21] He showed that the point of intersection in the red diagram exists at its proper location and can be determined automatically by computer algorithm. However, the applicability of the algorithm to real-world scenes is still questionable. In particular, uncertainties arise from noise, microtexture of the objects' surface, nonideal illumination of natural scenes, mutual illumination, and clipping at specular highlights,

```
01  input image
02  detect specular highlights
03  for all highlights do
04      extract 4 ROIs with corner placed at highlight
05      for all ROIs do
06          compute rg-diagram
07          compute Hough transform
08          detect local maxima
09          select candidate color lines
10          for all candidate color lines do
11              set start color to outmost color
12              repeat
13                  determine corresponding locations within ROI
14                  for all locations do
15                      for all path directions do
16                          search for longest path with end point near current location
17                          if path found
18                          then connect location to path
19                          else create new path of this direction with length one
20                      od
21                  od
22              until start color == end color
23          od
24          mark candidate color line with longest path
25      od
26      select marked candidate color line with longest path
27      if path longer than threshold
28      then accept selected color line and corresponding path
29      else reject
30  od
31  determine intersection
32  calculate scene-illuminant chomaticity from rg-values of intersection
```

Fig. 4. The CLS method of illuminant estimation in real-world scenes is visualized in pseudocode. The major parts of the algorithm—ROI detection, color line proposals, consistency check, and intersection estimation—are represented in lines 1–4, 5–9, 10–29, and 31–32, respectively.

which occur frequently in data taken from routine applications.

To obtain more general results, the validation of the CLS method must rely on real data. Although illuminant estimation using highlights is often applied in the field of color constancy research,[5,10,21,23,26] to the best of our knowledge, a standardized database of real-world images for validation does not exist. Most commonly, available databases are specific to a certain application. For example, the color constancy test images by Funt *et al.*[27] show macrotextured objects, and most of them are captured without specular highlights. Therefore they are unsuitable for our purposes. Furthermore, available databases often lack in documentation; in particular, any description of clipping at specular highlights is not provided.

A. Image Database

Inspired by the standard peppers image, we have built an image database from natural objects. This database is available from the authors on a noncommercial basis. Both IPS and CLS methods presuppose at least two objects of different color, which are illuminated by a single point source of light. If each object is unicolored, their reflections follow the dichromatic reflection model (3); i.e., the weight of the light source color varies as a result of the change of the normal direction of the objects' surface. This is shown to be valid for most nonmetal surfaces.[12]

Fruit and vegetables were placed on a black background without luster illuminated by a solidly mounted point light device (Storz Xenon Nova 20131520, Cologne, Germany), and were captured with a three-chip CCD camera (Lemke TC 804, Gröbenzell, Germany). In contrast with previously used images of artificial spheres,[17] natural objects neither are perfectly unicolored nor provide ideal smooth surfaces. We composed five ensembles, each of which contains at least four differently colored fruits or vegetables [Fig. 5(a)]. All ensembles were exposed from two camera positions with fixed position of the illuminant. This results in ten scenes.

Each scene was acquired with 368×278 pixels by averaging 20 frames in order to reduce imaging noise. According to Funt *et al.*,[27] the dynamic range was increased by floating-point capturing. To study clipping effects, we performed two kinds of calibration. First, the lightness of the illuminant was reduced as much as required to

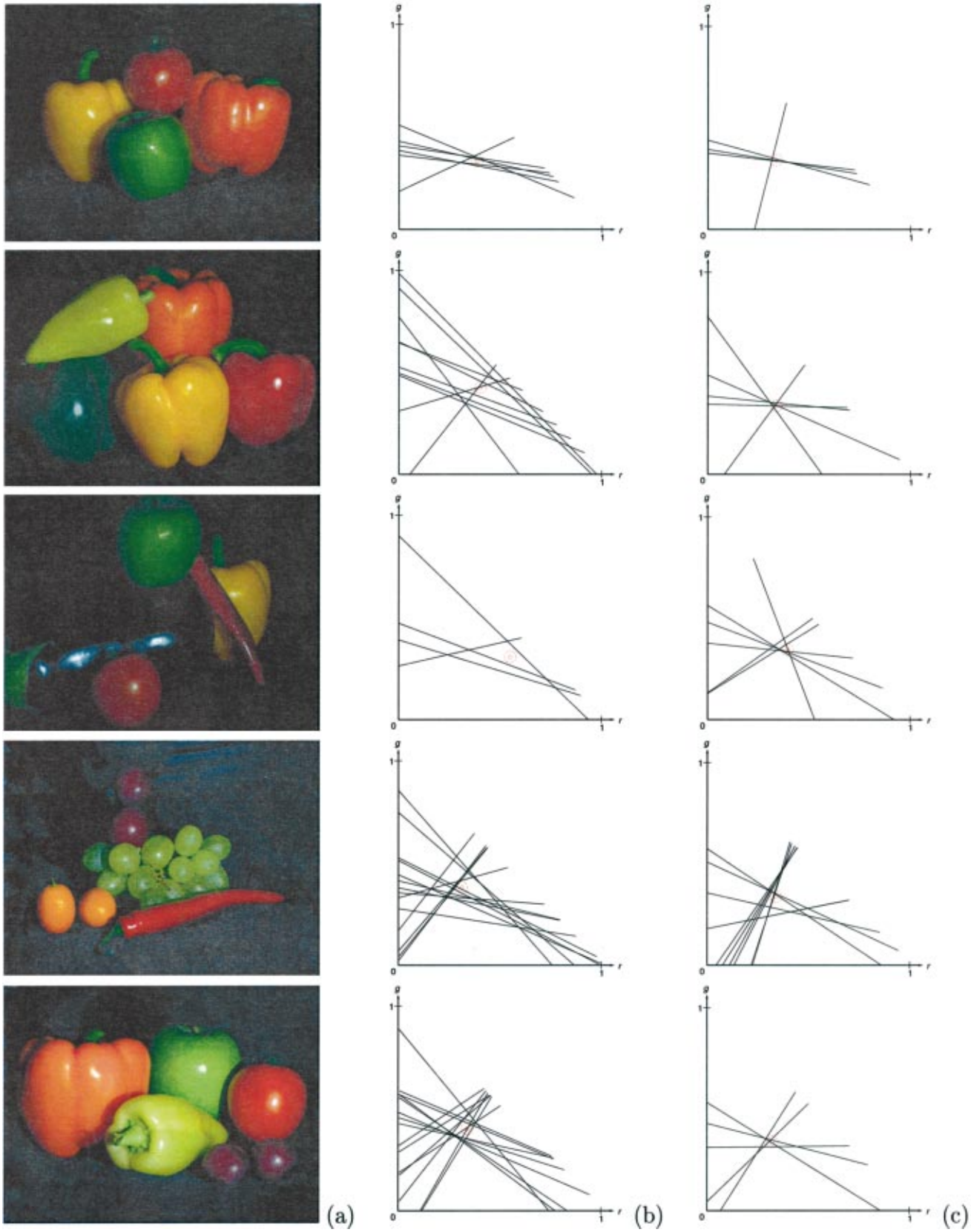

Fig. 5. (a) Arrangements of fruit and vegetables have been analyzed by (b) an IPS and (c) a CLS.

avoid clipping errors. Because of the mirroring surface of fruit, this results in roughly dark images. Second, adequate lightness was adjusted with respect to a human observer, and clipping in any color band was accepted.

Since illumination in real-world scenes is often nonideal, another set of 20 images has been captured. The Storz Nova lamp was replaced by a common light source, being less focused and strongly yellow colored. Altogether, 40 images have been used for validation.

B. Parameterization

With respect to the general applicability of IPS and CLS, a set of parameters have been determined for each method to enable reliable processing on the entire data set, regardless of light source or clipping effects. For the CLS implementation, the required path length was set to 6, accepting gaps of 2 or less pixels. Note that these parameters might vary within a broad range.

On the contrary, it was rather crucial to find a suitable set of parameters for the IPS algorithm. According to Eq. (7), color lines within the *rg* diagram are determined by slope a' and intercept b'. Because of the splitting of paths into an ascending and a descending part, which is denoted by the subscripts, as and des, respectively, a certain path is accepted only if both parts match sufficiently. Hence reliable color paths must satisfy

$$a'_{\mathrm{as}} - \frac{\alpha}{2}a'_{\mathrm{as}} < a'_{\mathrm{des}} < a'_{\mathrm{as}} + \frac{\alpha}{2}\alpha'_{\mathrm{as}},$$

$$b'_{\mathrm{as}} - \frac{\beta}{2}b'_{\mathrm{as}} < b'_{\mathrm{des}} < b'_{\mathrm{as}} + \frac{\beta}{2}b'_{\mathrm{as}} \qquad (11)$$

for $\alpha = 0.3$ and $\beta = 10\alpha$. In addition, minimal path lengths of 3 and 5 were required for the ascending and descending parts, respectively. This ensures at least two color paths in any of the 40 test images.

C. Experimental Results

Figures 5(b) and 5(c) show the color lines obtained from the IPS and CLS methods, respectively. In general, a CLS obviously tends to focus a point of intersection, while an IPS instead builds an area of intersection. Computation of the scene-illuminant chromaticity is quantitatively assessed by the coefficient of determination ρ^2 of the linear regression that is determined in the Hough space (see Subsection 2.D). This coefficient is defined between 0 and 1. A value of $\rho^2 = 1$ indicates that all data points are located exactly on the regression line. For example, in Fig. 5, $\rho^2 = 0.999909$ holds for the CLS in the second scene, while the IPS yields $\rho^2 = 0.880642$ in the fourth scene. In general, a CLS results in coefficients of determination that are close to 1.0, while ρ^2 is only approximately 0.9 if the color lines are detected by the IPS algorithm.

Although the actual color of both light sources is unknown, all scenes and camera positions must result in the same point of intersection (p_r, p_g) for the same illuminant. The mean coordinates of intersection, $\hat{p}_r$ and $\hat{p}_g$, as well as their standard deviations, σ_r and σ_g, respectively, have been computed based on $N \in \{3,7,10\}$ images with best quality ρ^2 for the unclipped and clipped data as well as for both illuminants.

Table 1 summarizes the results of our investigations. Concerning the CLS algorithm, reliable mean coordinates $(\hat{p}_r, \hat{p}_g)$ with small variances indicate robust chromaticity determination of both lamps. In addition, this robustness is emphasized by the mean coefficients of determination $\hat{\rho}^2$, which are always close to 1.0 and mostly have small variances. Obviously, the Storz Nova lamp is located near to the ideal white color $[(p_r, p_g) = (0.\overline{3}, 0.\overline{3})]$, while the other is more yellow colored $[(p_r, p_g) \approx (0.5, 0.4)]$. In contrast, an IPS yields fluctuating coordinates of intersection and lower coefficients of

Table 1. Mean Coordinates of Color Line Intersection $\hat{p}_r$ and $\hat{p}_g$ and Their Standard Deviations σ_r and σ_g for Each Scene Illuminator and Each Algorithm, Based on $N \in \{3,7,10\}$ Images with Best Quality, Where the Robustness is Indicated by the Mean Coefficient of Determination $\hat{\rho}^2$ and Its Corresponding Variance σ_ρ

	White Spot Illumination						Yellow Spot Illumination					
	IPS			CLS			IPS			CLS		
	3	7	10	3	7	10	3	7	10	3	7	10
N_{unclip}												
$\hat{p}_r$	0.3553	0.3343	0.3083	0.3326	0.3259	0.3224	0.3528	0.3932	0.3903	0.4355	0.4770	0.4902
$\hat{\sigma}_r$	0.0450	0.0427	0.0579	0.0169	0.0143	0.0158	0.0874	0.0947	0.0805	0.0438	0.0339	0.0542
$\hat{p}_g$	0.3600	0.3566	0.3547	0.3535	0.3477	0.3518	0.3703	0.3482	0.3423	0.4345	0.4247	0.4079
$\hat{\sigma}_g$	0.0158	0.0212	0.0190	0.0027	0.0066	0.0145	0.0233	0.0311	0.0282	0.0752	0.0534	0.0605
$\hat{\rho}^2$	0.8995	0.8412	0.7988	0.9999	0.9980	0.9894	0.8549	0.8271	0.7876	0.9998	0.9924	0.9834
σ_ρ	0.0264	0.0566	0.0857	0.0001	0.0022	0.0193	0.0340	0.0342	0.0734	0.0003	0.0119	0.0171
N_{clip}												
$\hat{p}_r$	0.3395	0.4143	0.3815	0.3178	0.3227	0.3186	0.5551	0.4871	0.4762	0.4710	0.5281	0.5524
σ_r	0.0225	0.1398	0.1296	0.0091	0.0250	0.0222	0.1199	0.1138	0.0982	0.0236	0.1254	0.1056
$\hat{p}_g$	0.3552	0.3421	0.3558	0.3231	0.3322	0.3300	0.3383	0.3551	0.3601	0.4264	0.3527	0.3712
σ_g	0.0171	0.0537	0.0514	0.0190	0.0162	0.0186	0.0661	0.0461	0.0441	0.0176	0.0891	0.0820
$\hat{\rho}^2$	0.9719	0.9520	0.9347	0.9999	0.9980	0.9938	0.9590	0.9437	0.9258	0.9976	0.9840	0.9494
σ_ρ	0.0032	0.0203	0.0323	0.0000	0.0022	0.0089	0.0048	0.0154	0.0342	0.0025	0.0151	0.0771

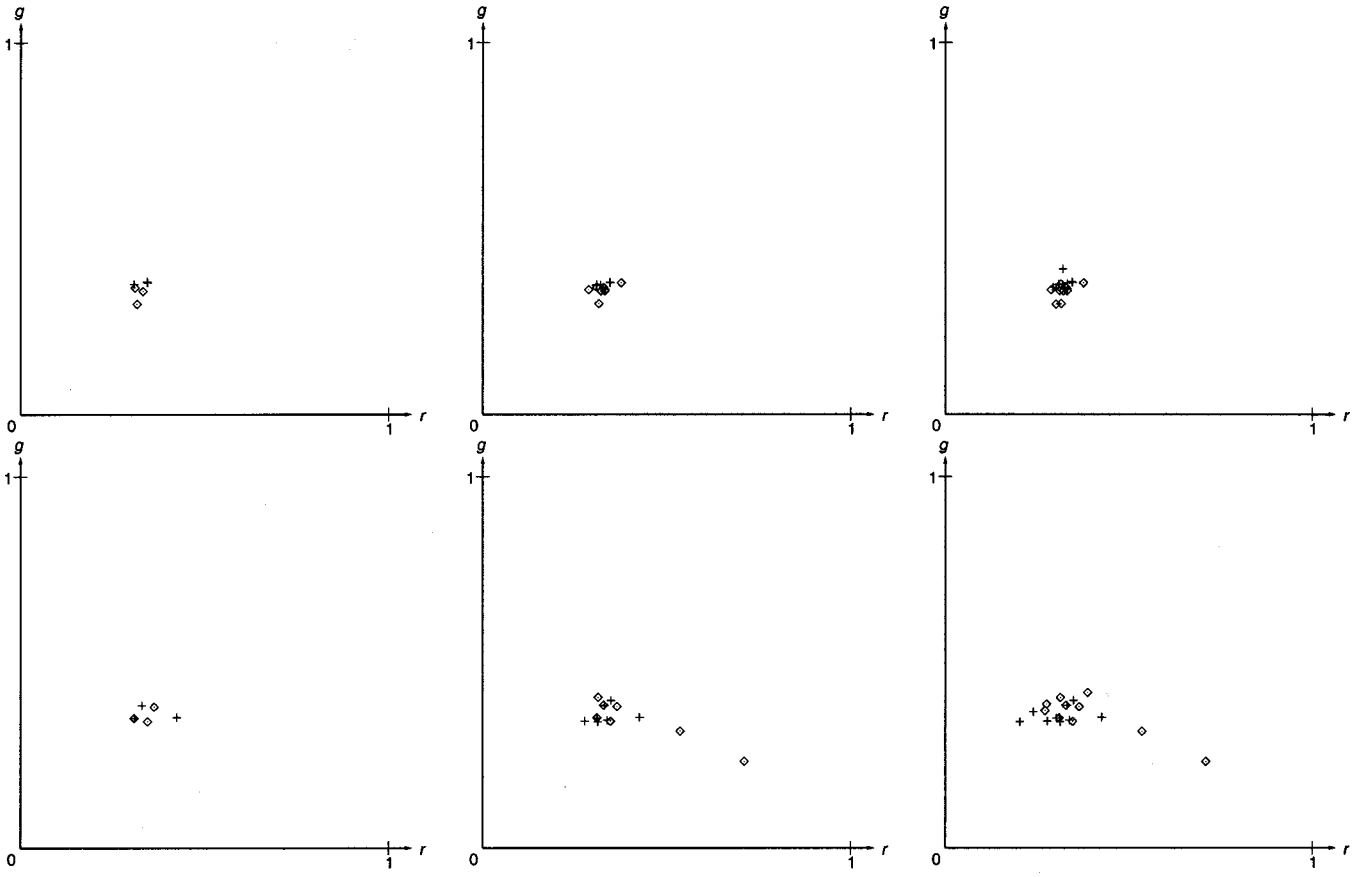

Fig. 6. According to Table 1, the illuminant chromaticity of the white lamp is determined from the $N \in \{3,7,10\}$ most reliable test images. Data obtained from unclipped and clipped capturing are denoted by crosses and rhombs, respectively. The upper and lower rows correspond to the CLS and IPS methods, respectively. Note that CLS clusters are substantially smaller.

determination with larger variances. In the case of the unclipped data, which perfectly supports the dichromatic reflection model, the IPS method is particularly less precise and less robust.

D. Data Analysis

Based on the data sets with $N = 10$ measures (Table 1), statistical analyses were performed. For all tests (white lamp, yellow lamp, clipped data, unclipped data), a global niveau of $\alpha = 0.05$ was selected. Based on each of the two coordinates of the resulting mean intersection, the methods (IPS versus CLS) and the acquisition techniques (unclipped versus clipped) were compared. In addition, the coefficient of determination was used to assess the robustness. Hence all images were used in $P = 5$ tests. According to the α adjustment by Bonferroni, all tests were designed at the level of $\alpha/P = 0.01$.

To determine whether the robustness of CLS is superior to that of IPS, we applied a Wilcoxon signed rank test to the coefficients of determination. In the case of unclipped images ($N_{\text{unclip}} = 10$), ρ^2 was found to be significantly higher for the CLS method than for the IPS method ($p < 0.01$). This result holds for both sources of illumination. In the case of clipped images ($N_{\text{clip}} = 10$), significance was found only for white illumination ($p < 0.01$) and not for the yellow-light source ($p > 0.01$). Nevertheless, these results verify the improved robustness of the CLS method, which is qualitatively indicated by Fig. 6.

A second analysis was designed to assess the equivalence of the methods. In the case of failure of either method, significant differences in the coordinates of intersection were expected. Concerning evidence for the normal distribution, the Student's t test for paired data was applied to the differences of each of the coordinates. Concerning white illumination, no significant differences were found between both methods ($p > 0.01$) for unclipped ($N_{\text{unclip}} = 10$) as well as clipped ($N_{\text{clip}} = 10$) images. In contrast, the illuminant chromaticity of the yellow-colored lamp differs significantly ($p < 0.01$) in both coordinates for unclipped images ($N_{\text{unclip}} = 10$). Here the robustness of IPS ($\hat{\rho}^2 = 0.78$) is substantially lower than that of CLS ($\hat{\rho}^2 = 0.98$), which indicates a failure of the IPS method. Concerning the clipped data ($N_{\text{clip}} = 10$), the same result holds only for the r coordinate ($p < 0.01$) and not for the g coordinate ($p > 0.01$). Since unclipped data are noisier than clipped data and yellow illuminants are more difficult to determine than white-light sources (see Section 4), this result again confirms the impact obtained with the CLS approach.

A last investigation was carried out to assess the effect of data clipping with respect to the precision of illuminant

chromaticity determination when using the CLS method. A Student's t test for unpaired data was performed for each of the coordinates. For both illuminations, the differences in both coordinates were insignificant ($p > 0.01$). Although this insignificance does not prove identical distributions for clipped and unclipped data, one may deduce that the effect of data clipping is minor and hence that the CLS method is applicable to any scene, with certain precautions.

4. DISCUSSION

Real-world scenes are usually acquired by standard CCD cameras. Often, there is no choice in use of the scene's illuminator, and hence its color is unknown. Therefore the image itself must be used to estimate the chromaticity of the scene's illuminant. Note that this calibration is required for any subsequent procedure of color quantification. Nevertheless, an ideal white-colored illuminant is assumed for simplicity in several applications, or the color constancy problem is thoroughly ignored.

Approximately 15 years ago, Lee introduced a theory and a method of data-based illuminant color determination.[21] The initial IPS algorithm was shown to perform sufficiently only if restrictive assumptions hold on surface homogeneity and dichromatic reflectance. In particular, the IPS method is not robust against disturbances such as noise, interreflections, and textured objects, which often occur in real applications. This was confirmed by our investigation. In contrast, the CLS method of color line determination has been shown to significantly improve precision and robustness. As a result, a CLS is applicable to noisy images and scenes of objects with microtextured surfaces regardless of local sensor saturation.

Figure 6 visualizes the left-hand part of Table 1. A CLS forms small and circular clusters for $N \in \{3,7,10\}$ (upper row) regardless of whether the intersection is based on unclipped or clipped data (which are marked with crosses and rhombs, respectively). The corresponding results from an IPS are visualized in the lower row of Fig. 6. Note that the IPS clusters are widespread and elliptical rather than circular. The principal axis of each elliptical cluster is approximately parallel to the r axis. In other words, the p_r coordinate obtained by the IPS algorithm is disturbed more frequently. Note that this correlates with our statistical analysis (see Subsection 3.D). If we refer to Fig. 5(b), the reason for this shortcoming of the IPS algorithm is obvious. A larger number of color lines is directed along the r axis. In addition, several lines are located close to the diagonal from $(r,g) = (1,0)$ to (0,1). Those lines result from interreflections at object borders that are accepted only by Lee's IPS method and not by our CLS approach.

Concerning the IPS method on clipped data, the points of intersection are detected more reliably ($\hat{\rho}^2 > 0.9$) as compared with the method on unclipped data ($\hat{\rho}^2 < 0.8$). This is caused by the increased signal-to-noise ratio, yielding longer descending parts of IPS color paths. However, improved reliability does not coincide with increased precision. In the case of clipped data, the detection of the ascending part of IPS color paths often fails. Therefore a high variance of measures is obtained (Table 1), which is visualized by the enlarged cluster size of rhombs as compared with that of crosses (Fig. 6, lower row).

In our analysis, the results obtained from the white illumination have been proven more reliable than those obtained from the yellow-colored source of light. On the one hand, this is caused by the enlarged focus of the yellow lamp. On the other hand, yellow is a mixture of red and green. Therefore the difference between body and surface reflection is reduced on red, green, and also orange objects. Hence minor estimation errors have major effects on the color line parameters. Furthermore, the lack of short-illumination wavelengths reduces the number of reliable color lines obtained from blue surfaces, because the reflection of blue surfaces is limited by the intensity of the blue component of the illuminant. Since these lines are directed in the rg diagram from $(r,g) = (0,0)$ toward (1,1), they are important for a sharply focused point of intersection in the color diagram.

Another limit of the proposed algorithm may result from the simple threshold technique that is used to determine the ROIs around specular highlights. Note that the simplified definition of saturation in Eqs. (9) is not meaningful as such because it does not have any chromatic adaptation mechanism and it is implicitly assumed that the images have been correctly color balanced. Hence any selection of the thresholds in Eqs. (9) carries the risk of excluding strongly colored illuminants. However, such fundamental failures of the CLS approach have not been observed in real-world scenes.

5. CONCLUSION

In this paper, we have proposed the algorithm of color line search (CLS) to estimate the chromaticity of a single point source of light from a single color image. Our CLS method applies standard techniques, such as Hough and Karhunen–Loève transforms, but does not require difficult preprocessing steps such as knowledge-based segmentation or other high-level image analyses. Information about the color of the illuminant is extracted from highlighted regions that can be located easily at colored surfaces by simple thresholding. We have evaluated the method on real-world scenes with statistically reliable results. Both stability and accuracy are significantly improved as compared with those of the former method of image path search (IPS). Therefore the CLS method is suitable for a wide range of applications.

The CLS method can be upgraded to scenes of objects with only macrotextured surfaces if gaps of more than 2 pixels in the image paths are allowed during the consistency check. However, this will require a more sophisticated consistency check procedure. Nevertheless, the normalized colors obtained from any surface should induce a certain line in the rg diagram to validate the dichromatic reflection model. With such an extension, image-based illuminant estimation is no longer restricted to scenes of objects with homogeneous surfaces.

APPENDIX A: DERIVATION OF EQUATIONS (5)

To derive Eqs. (5), we start from the three linear equations

$$\begin{aligned} R &= w_s\beta_s s^R + w_b\beta_b^R s^R, \\ G &= w_s\beta_s s^G + w_b\beta_b^G s^G, \\ B &= w_s\beta_s s^B + w_b\beta_b^B s^B, \end{aligned} \tag{A1}$$

which describe the dichromatic reflection model [Eq. (3)]. Normalization of the blue channel in Eqs. (A1) to the red one gives

$$\frac{B}{R} = \frac{w_s\beta_s s^B + w_b\beta_b^B s^B}{w_s\beta_s s^R + w_b\beta_b^R s^R}. \tag{A2}$$

We extend the fraction in Eq. (A2) by the term $(\beta_b^G - \beta_b^R)s^G$, resolve the bracketed expressions in the dividend, and obtain

$$\frac{B}{R} = \frac{(w_s\beta_s s^B + w_b\beta_b^B s^B)(\beta_b^G - \beta_b^R)s^G}{(w_s\beta_s s^R + w_b\beta_b^R s^R)(\beta_b^G - \beta_b^R)s^G} = \frac{w_s\beta_s\beta_b^G s^G s^B + w_b\beta_b^G\beta_b^B s^G s^B - w_s\beta_s\beta_b^R s^G s^B - w_b\beta_b^R\beta_b^B s^G s^B}{(w_s\beta_s s^R + w_b\beta_b^R s^R)(\beta_b^G - \beta_b^R)s^G}. \tag{A3}$$

Factoring out the terms $(\beta_b^G - \beta_b^R)s^B$ and $s^G s^B$ in Eq. (A3) yields

$$\frac{B}{R} = \frac{(w_s\beta_s s^G + w_b\beta_b^G s^G)(\beta_b^B - \beta_b^R)s^B}{(w_s\beta_s s^R + w_b\beta_b^R s^R)(\beta_b^G - \beta_b^R)s^G} + \frac{(w_s\beta_s\beta_b^G - w_s\beta_s\beta_b^B + w_b\beta_b^R\beta_b^G - w_b\beta_b^R\beta_b^B)s^G s^B}{(w_s\beta_s s^R + w_b\beta_b^R s^R)(\beta_b^G - \beta_b^R)s^G}. \tag{A4}$$

We cancel out s^G in the second addend, extend by s^R, and factor out $\beta_b^G - \beta_b^B$ in Eq. (A4) to obtain

$$\frac{B}{R} = \frac{(w_s\beta_s s^G + w_b\beta_b^G s^G)(\beta_b^B - \beta_b^R)s^B}{(w_s\beta_s s^R + w_b\beta_b^R s^R)(\beta_b^G - \beta_b^R)s^G} + \frac{(w_s\beta_s s^R + w_b\beta_b^R s^R)(\beta_b^G - \beta_b^B)s^B}{(w_s\beta_s s^R + w_b\beta_b^R s^R)(\beta_b^G - \beta_b^R)s^R}. \tag{A5}$$

In Eq. (A5), we are able to cancel out the bracketed expression in the second addend. This results in the form of a straight line [Eq. (4)]. Slope a and intercept b are given by Eqs. (5):

$$\begin{aligned} \frac{B}{R} &= \frac{(\beta_b^B - \beta_b^R)s^B}{(\beta_b^G - \beta_b^R)s^G}\frac{(w_s\beta_s s^G + w_b\beta_b^G s^G)}{(w_s\beta_s s^R + w_b\beta_b^R s^R)} + \frac{(\beta_b^G - \beta_b^B)s^B}{(\beta_b^G - \beta_b^R)s^R} \\ &= a\frac{G}{R} + b \end{aligned}$$

with

$$a = \frac{s^B}{s^G}\frac{\beta_b^B - \beta_b^R}{\beta_b^G - \beta_b^R}, \qquad b = \frac{s^B}{s^R}\frac{\beta_b^G - \beta_b^B}{\beta_b^G - \beta_b^R}. \qquad \square$$

APPENDIX B: DERIVATION OF EQUATION (7)

To derive Eq. (7), we start again from the three linear equations (A1) but normalize the green channel to the sum of red, green, and blue. This yields

$$\frac{G}{R + G + B} = \frac{w_s\beta_s s^G + w_b\beta_b^G s^G}{R + G + B}. \tag{B1}$$

We extend the fraction in Eq. (B1) with the term $(\beta_b^B s^B - \beta_b^R s^B + \beta_b^G s^G - \beta_b^R s^G)s^R$, split the fraction, and factor out the terms $(\beta_b^B - \beta_b^G)s^G s^B$ and $(\beta_b^G - \beta_b^R)s^R s^G$ to obtain

$$\begin{aligned} \frac{G}{R + G + B} &= \frac{(w_s\beta_s s^G + w_b\beta_b^G s^G)(\beta_b^B s^B - \beta_b^R s^B + \beta_b^G s^G - \beta_b^R s^G)s^R}{(R + G + B)(\beta_b^B s^B - \beta_b^R s^B + \beta_b^G s^G - \beta_b^R s^G)s^R} \\ &= \frac{(\beta_b^B - \beta_b^G)s^G s^B(w_s\beta_s s^R + w_b\beta_b^R s^R)}{(R + G + B)(\beta_b^B s^B - \beta_b^R s^B + \beta_b^G s^G - \beta_b^R s^G)s^R} \\ &\quad + \frac{(\beta_b^G - \beta_s^R)s^R s^G[(w_s\beta_s s^G + w_b\beta_b^G s^G) + (w_s\beta_s s^B + w_b\beta_b^B s^B)]}{(R + G + B)(\beta_b^B s^B - \beta_b^R s^B + \beta_b^G s^G - \beta_b^R s^G)s^R}. \end{aligned} \tag{B2}$$

Factoring out s^R in Eq. (B2) and substituting the expressions from Eqs. (A1) for R, G, and B yield

$$\frac{G}{R + G + B} = \frac{s^R s^G\left[(\beta_b^G - \beta_b^R)(G + B) + \frac{s^B}{s^R}(\beta_b^B - \beta_b^G)R\right]}{(R + G + B)(\beta_b^B s^B - \beta_b^R s^B + \beta_b^G s^G - \beta_b^R s^G)s^R}. \tag{B3}$$

A division by the term $s^R s^G(\beta_b^G - \beta_b^R)$ in Eq. (B3) holds:

$$\frac{G}{R+G+B} = \frac{(R+G+B) + \left[-1 + \frac{s^B(\beta_b^B - \beta_b^G)}{s^R(\beta_b^G - \beta_b^R)}\right]R}{(R+G+B)\left[\frac{\beta_b^B s^B - \beta_b^R s^B + \beta_b^G s^G - \beta_b^R s^G}{s^G(\beta_b^G - \beta_b^R)}\right]}. \tag{B4}$$

Now we split the fraction in Eq. (B4) and factor out the term $s^B(\beta_b^B - \beta_b^R)$ in the divisor to obtain the straight line form Eq. (7) with slope a' and ordinate intercept b':

$$\frac{G}{R+G+B} = \frac{\left[-1 + \frac{s^B(\beta_b^B - \beta_b^G)}{s^R(\beta_b^G - \beta_b^R)}\right]R}{(R+G+B)\left[1 + \frac{s^B(\beta_b^B - \beta_b^R)}{s^G(\beta_b^G - \beta_b^R)}\right]} + \frac{1}{1 + \frac{s^B(\beta_b^B - \beta_b^R)}{s^G(\beta_b^G - \beta_b^R)}} = a'\frac{R}{R+G+B} + b'$$

with

$$a' = -\left[1 - \frac{s^B(\beta_b^B - \beta_b^G)}{s^R(\beta_b^G - \beta_b^R)}\right] \Big/ \left[1 + \frac{s^B(\beta_b^B - \beta_b^R)}{s^G(\beta_b^G - \beta_b^R)}\right],$$

$$b' = 1\left[1 + \frac{s^B(\beta_b^B - \beta_b^R)}{s^G(\beta_b^G - \beta_b^R)}\right].$$

□

APPENDIX C: PROOF OF EQUATIONS (8)

The intersection of two color lines in the *rg* diagram at $(r, g) = (p_r, p_g)$, which results from objects with another spectral emission, is given by Eq. (7):

$$p_g = a' p_r + b'. \tag{C1}$$

The replacement of a', b', and p_r in Eq. (C1) by their definitions from Eqs. (7) and (8) yields

$$p_g = \frac{s^R\left[-1 + \frac{s^B(\beta_b^B - \beta_b^G)}{s^R(\beta_b^G - \beta_b^R)}\right]}{(s^R + s^G + s^B)\left[1 + \frac{s^B(\beta_b^B - \beta_b^R)}{s^G(\beta_b^G - \beta_b^R)}\right]} + \frac{1}{1 + \frac{s^B(\beta_b^B - \beta_b^R)}{s^G(\beta_b^G - \beta_b^R)}}. \tag{C2}$$

Unifying both divisors in Eq. (C2) by extension of the second fraction with the term $s^R + s^G + s^B$ results in

$$p_g = \frac{\left[-1 + \frac{s^B(\beta_b^B - \beta_b^G)}{s^R(\beta_b^G - \beta_b^R)}\right]s^R + (s^R + s^G + s^B)}{(s^R + s^G + s^B)\left[\frac{\beta_b^B s^B - \beta_b^R s^B + \beta_b^G s^G - \beta_b^R s^G}{s^G(\beta_b^G - \beta_b^R)}\right]}. \tag{C3}$$

By an extension with the term $s^G(\beta_b^G - \beta_b^R)$, we simplify the double fractions in Eq. (C3) and obtain

$$p_g = \frac{s^G[-s^R(\beta_b^G - \beta_b^R) + s^B(\beta_b^B - \beta_b^G)] + (\beta_b^G - \beta_b^R)(s^R + s^G + s^B)}{(s^R + s^G + s^B)(\beta_b^B s^B - \beta_b^R s^B + \beta_b^G s^G - \beta_b^R s^G)}. \tag{C4}$$

We factor out the term $s^G/(s^R + s^G + s^B)$ and resolve the multiplication. This yields

$$p_g = \frac{s^G}{s^R + s^G + s^B}\frac{-\beta_b^G s^R + \beta_b^R s^R + \beta_b^B s^B - \beta_b^G s^B + \beta_b^G s^R + \beta_b^G s^G + \beta_b^G s^B - \beta_b^R s^R - \beta_b^R s^G - \beta_b^R s^B}{\beta_b^B s^B - \beta_b^R s^B + \beta_b^G s^G - \beta_b^R s^G}$$
$$= \frac{s^G}{s^R + s^G + s^B}\frac{\beta_b^B s^B + \beta_b^G s^G - \beta_b^R s^G - \beta_b^R s^B}{\beta_b^B s^B - \beta_b^R s^B + \beta_b^G s^G - \beta_b^R s^G} = \frac{s^G}{s^R + s^G + s^B}.$$

□

ACKNOWLEDGMENT

The authors thank Ralph Minkenberg, Institute of Biometry, RWTH Aachen, Germany, for his assistance in performing the statistical analysis.

Address correspondence to Thomas M. Lehmann at the address on the title page or by phone, 49-241-80 88793; fax, 49-241-80-82426; or e-mail, lehmann@computer.org.

REFERENCES

1. D. H. Brainard, "Color constancy in the nearly natural image. 2. Achromatic loci," J. Opt. Soc. Am. A **15**, 307–325 (1998).
2. I. Kuriki and K. Uchikawa, "Limitations of surface-color and apparent-color constancy," J. Opt. Soc. Am. A **13**, 1622–1636 (1996).
3. K.-H. Bäuml, "Color constancy: the role of image surface in illuminant adjustment," J. Opt. Soc. Am. A **16**, 1521–1530 (1999).
4. E. W. Jin and S. K. Shevell, "Color memory and color constancy," J. Opt. Soc. Am. A **13**, 1981–1991 (1996).
5. M. D'Zmura and P. Lennie, "Mechanisms of color constancy," J. Opt. Soc. Am. A **3**, 1662–1672 (1986).
6. M. D'Zmura and G. Iverson, "Color constancy. III. General linear recovery of spectral descriptions for lights and surfaces," J. Opt. Soc. Am. A **11**, 2389–2400 (1994).
7. D. H. Brainard and W. T. Freeman, "Bayesian color constancy," J. Opt. Soc. Am. A **14**, 1393–1411 (1997).
8. S. Tominaga, "Multichannel vision system for estimating surface and illuminant functions," J. Opt. Soc. Am. A **13**, 2163–2173 (1996).
9. J. Ho, B. V. Funt, and M. S. Drew, "Separating a color signal into illumination and surface reflectance components: theory and applications," IEEE Trans. Pattern Anal. Mach. Intell. **12**, 966–977 (1990).
10. S. Tominaga and B. A. Wandell, "Standard surface-reflection model and illuminant estimation," J. Opt. Soc. Am. A **6**, 576–584 (1989).
11. S. Tominaga and B. A. Wandell, "Component estimation of surface spectral reflectance," J. Opt. Soc. Am. A **7**, 312–317 (1990).
12. S. Tominaga, "Surface identification using the dichromatic reflection model," IEEE Trans. Pattern Anal. Mach. Intell. **13**, 658–670 (1991).
13. G. Healey and D. Slater, "Global color constancy: recognition of objects by use of illumination-invariant properties of color distributions," J. Opt. Soc. Am. A **11**, 3003–3010 (1994).
14. B. V. Funt and G. D. Finlayson, "Color constant color indexing," IEEE Trans. Pattern Anal. Mach. Intell. **17**, 522–533 (1995).
15. L. T. Maloney and B. A. Wandell, "Color constancy: a method for recovering surface spectral reflectances," J. Opt. Soc. Am. A **3**, 29–33 (1986).
16. C. L. Novak and S. A. Shafer, "Supervised color constancy using a color chart," Tech. Rep. CMU-CS-90-140 (School of Computer Science, Carnegie Mellon University, Pittsburgh, Pa., 1990).
17. C. Palm, I. Scholl, T. Lehmann, and K. Spitzer, "Quantitative color measurement in laryngoscopic images," in *POSTER98* (Faculty of Electrical Engineering, Czech Technical University, Prague, 1998), Paper NS22.
18. H. Hassan, J. Ilgner, C. Palm, T. Lehmann, K. Spitzer, and M. Westhofen, "Objective judgement in laryngoscopic images," in *Advances in Quantitative Laryngoscopy, Voice and Speech Research*, T. Lehmann, C. Palm, K. Spitzer, and T. Tolxdorff, eds. (RWTH, Aachen, Germany, 1998), pp. 135–142.
19. G. Buchsbaum, "A spatial processor model for object colour perception," J. Franklin Inst. **300**, 1–26 (1980).
20. E. H. Land, "Recent advances in retinex theory," Vision Res. **26**, 7–21 (1986).
21. H.-C. Lee, "Method for computing scene-illuminant chromaticity from specular highlights," J. Opt. Soc. Am. A **3**, 1694–1699 (1986).
22. S. A. Shafer, "Using color to separate reflection components," Color Res. Appl. **10**, 210–218 (1985).
23. M. H. Brill, "Image segmentation by object color: a unifying framework and connection to color constancy," J. Opt. Soc. Am. A **7**, 2041–2047 (1990).
24. B. V. Funt and M. S. Drew, "Color space analysis of mutual illumination," IEEE Trans. Pattern Anal. Mach. Intell. **15**, 1319–1326 (1993).
25. V. F. Leavers, *Shape Detection in Computer Vision Using the Hough Transform* (Springer-Verlag, Berlin, 1992).
26. Y.-L. Tian and H. T. Tsui, "Shape from shading for non-Lambertian surfaces from one color image," in *Proceedings of the 13th International Conference on Pattern Recognition* (IEEE Computer Society, Los Alamitos, Calif., 1996), Vol. 1, pp. 258–262.
27. B. Funt, K. Barnard, and L. Martin, "Is machine colour constancy good enough?" in *Proceedings of the 5th European Conference on Computer Vision* (Springer-Verlag, Berlin, 1998), Vol. 1, pp. 445–459.